npj | 2D materials and applications

www.nature.com/npj2dmaterials

ARTICLE OPEN

Insulator–metal transition in $CrSiTe_3$ triggered by structural distortion under pressure

J. L. Musfeldt[1,2]✉, D. G. Mandrus[3,4] and Z. Liu[5]

van der Waals solids are well known to host remarkable phase diagrams with competing phases, unusual energy transfer processes, and elusive states of matter. Among this class of materials, chalcogenides have emerged as the most flexible and relevant platforms for unraveling charge–structure–function relationships. In order to explore the properties of complex chalcogenides under external stimuli, we measured the far infrared spectroscopic response of $CrSiTe_3$ under extreme pressure–temperature conditions. Analysis of the 368 cm^{-1} Si–Te stretching mode and the manner in which it is screened by the closure of the indirect gap reveals that the insulator–metal transition takes place immediately after the structural phase transition—once the mixed phase aspect of the lattice distortion is resolved. At the same time, the two-phase region associated with the structural transition widens with decreasing temperature, and the slope of the insulator–metal transition under pressure is consistent with increasing entropy. These trends completely revise the character of the temperature–pressure phase diagram as well as the relationship between the structural and insulator–metal transitions, leading to a critical nexus of activity that may hide a quantum critical point and allow superconductivity to emerge.

npj 2D Materials and Applications (2023)7:28 ; https://doi.org/10.1038/s41699-023-00389-x

INTRODUCTION

Complex chalcogenides are exceptionally responsive to external stimuli. Under compression, systems like $CrSiTe_3$, $FePS_3$, $MnPS_3$, and $CrGeTe_3$ host layer sliding, insulator–metal transitions, magnetic dimensionality crossovers, piezochromism, the possibility of orbital-selective Mott and polar metal states, and superconductivity[1–22]. The 33 K ferromagnet $CrSiTe_3$ has earned widespread recognition for remarkable properties in both single crystal and monolayer form[23–27]. The discovery of pressure-induced superconductivity above 7.5 GPa and below 4.2 K is one of these exciting developments[27]. Establishing the local lattice distortions and the precise relationship between the structural and insulator–metal transitions is crucial to unraveling how superconductivity develops and distinguishing between conventional vs. unconventional mechanisms in this class of materials. At the same time, $CrSiTe_3$ is a layered van der Waals material that has attracted extraordinary attention for the demonstration of single-layer ferromagnetism and current-driven control of the spin state[26,28–34]. Whether superconductivity arises in the ultrathin limit is currently unexplored, although the fact that the Curie temperature T_C rises with decreasing layer number as well as under strain and pressure[30,31,34] suggests that the superconducting transition temperature might do so as well[35,36]. Further developing the phase diagram and resolving the connection between the structural and insulator–metal transitions as well as the intersection of competing phases is a significant step toward evaluating such a relationship.

In order to explore these themes in a complex chalcogenide, we combined synchrotron-based infrared spectroscopy and diamond anvil cell techniques to measure the far-infrared response of $CrSiTe_3$ under extreme pressure–temperature conditions. Because closing an indirect gap screens the phonons much less effectively than closing a direct gap, we can follow the evolution of the phonons into the metallic state. The ^2E_u symmetry Si–Te stretching mode at 368 cm^{-1}—noteworthy for engaging in spin-phonon coupling across the magnetic ordering transition[23]—is particularly informative in this regard. This vibrational mode hardens strongly on approach to the pressure-driven structural transition, broadens and develops weak doublet character in the mixed-phase region, and rides on top of a gradually increasing electronic background as the indirect gap begins to close. In the end, the insulator–metal transition is swift and sharp. What differentiates our work from previous results is the finding that the first-order structural phase transition in $CrSiTe_3$ is triggered before (but in close proximity to) the insulator–metal transition. The latter is set in motion almost immediately afterward. With decreasing temperature, the two-phase region associated with the structural transition broadens, and the insulator–metal transition shifts to slightly higher pressure, indicative of a positive entropy change. Our findings run counter to previous results[27] and completely revise the entire character of the temperature–pressure (T–P) phase diagram for this compound. These trends also open the possibility that the juxtaposition of events both hides a quantum critical point and lays the foundation for superconductivity.

RESULTS AND DISCUSSION

Spectroscopic signatures of the structural and insulator–metal transitions

Figure 1a displays the infrared response of $CrSiTe_3$ at ambient conditions inside the diamond anvil cell. Three infrared-active vibrational modes are observed. We assign the peak near 90 cm^{-1} as an A_u symmetry Te displacement mode, the feature near 215 cm^{-1} as an ^1E_u symmetry Te–Cr–Te bending mode, and the peak at 368 cm^{-1} as a ^2E_u symmetry Si–Te stretching mode. All of these features harden significantly under pressure. In order to understand the local lattice distortions associated with the structural

---

[1]Department of Chemistry, University of Tennessee, Knoxville, TN 37996, USA. [2]Department of Physics and Astronomy, University of Tennessee, Knoxville, TN 37996, USA. [3]Department of Materials Science and Engineering, University of Tennessee, Knoxville, TN 37996, USA. [4]Materials Science and Technology Division, Oak Ridge National Laboratory, Oak Ridge, TN 37831, USA. [5]Department of Physics, University of Illinois Chicago, Chicago, IL 60607-7059, USA. ✉email: musfeldt@utk.edu

phase transition, we track the frequency shifts and splittings of these phonons as a function of pressure. The behavior of the Si–Te stretching mode determines the location of the structural phase transition. We find that weak doublet character signals a mixed phase region that persists over a broad pressure range [Fig. 1c]. Oscillator fits of the Si–Te phonon reveal where the process begins and ends. The insulator–metal transition is different. Due to the superior stability and brightness of the synchrotron source, we can measure absorption very close to the metallic transition—even though the signal is low—and we can follow the entire transition into the metallic phase because $CrSiTe_3$ is a bad metal with an indirect gap. As an additional check, we monitor the emerging metallicity with complementary reflectance spectroscopy. Both techniques provide similar estimates of the critical pressure for the insulator–metal transition.

Sequence of pressure-driven transitions in $CrSiTe_3$ at room temperature

The behavior of the 368 cm^{-1} Si–Te stretching mode is particularly revealing [Fig. 1b, c]. In addition to hardening strongly under pressure ($\partial\omega/\partial P$ = 3.4 cm^{-1}/GPa at 300 K), the Si–Te stretch broadens considerably between approximately 6 and 8 GPa and displays a poorly resolved doublet structure. Oscillator fits of these features are shown in the Supporting information. This broadening and eventual peak separation could be a signature of (i) weak symmetry breaking or (ii) a mixed phase regime. There are two pieces of evidence that point toward the latter scenario. First, the character of the frequency vs. pressure plot in Fig. 1c is consistent with phase coexistence. Second, the x-ray diffraction data of Cai et al. provide clear evidence for a sluggish structural phase transition between $R\bar{3}$ and a high-pressure phase over the

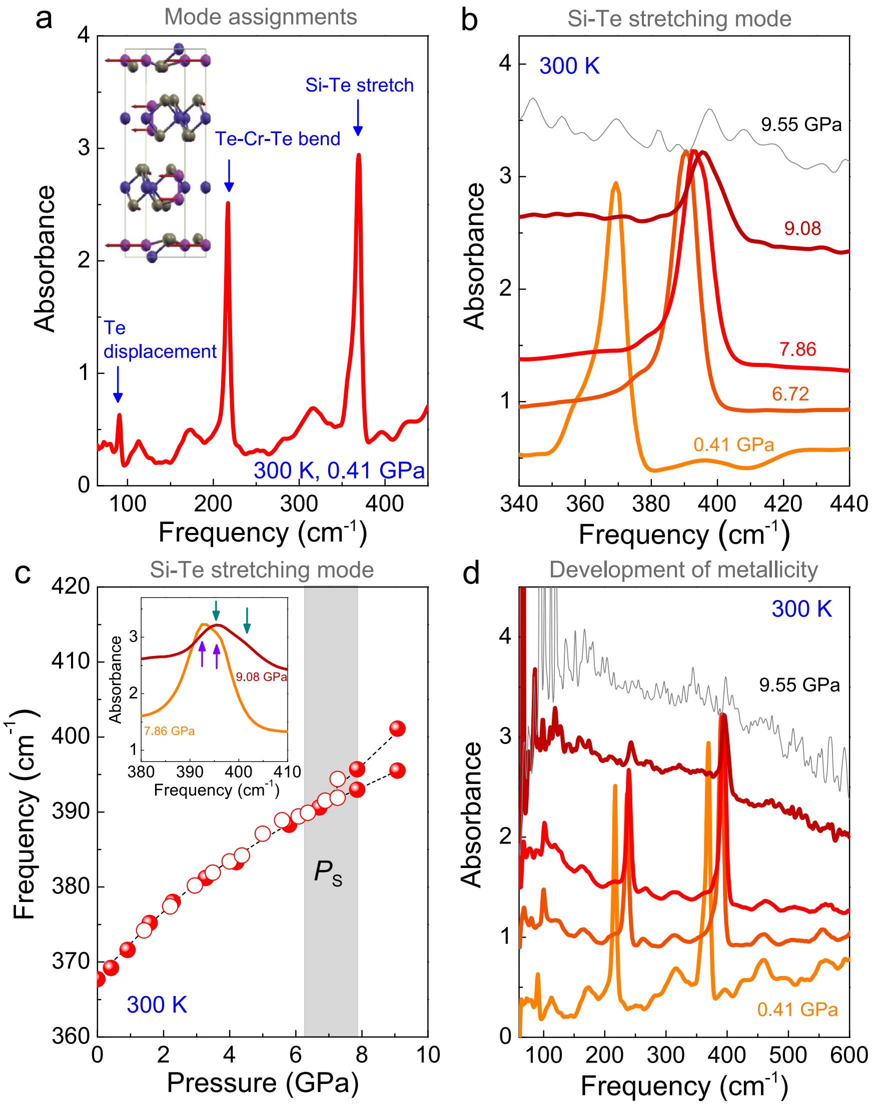

Fig. 1 Infrared response of $CrSiTe_3$ under pressure. **a** Infrared spectrum of $CrSiTe_3$ inside the diamond anvil cell at 300 K. Based upon an $R\bar{3}$ space group, this van der Waals material hosts three infrared-active phonon modes. The 368 cm^{-1} Si–Te stretching mode is strongly coupled to the 33 K ferromagnetic ordering transition[23]. Inset: calculated displacement pattern for the Si–Te stretching mode at 368 cm^{-1} reproduced from ref. [23]. This displacement modulates the Te centers in the 90° Cr–Te–Cr superexchange pathway. **b** Close-up view of the Si–Te stretching mode showing the development of the first-order structural phase transition, the rising absorption background, and metallicity. **c** Frequency vs. pressure plot of the Si–Te stretching mode at room temperature. The closed and open symbols correspond to two different runs. The mixed phase region associated with the structural phase transition is indicated in gray. Inset: close-up view of the Si–Te stretch showing the development of doublet character due to the presence of two coexisting phases. **d** Spectral evidence for the insulator–metal transition due to closure of the indirect gap near 9.55 GPa (indicated in gray). The spectra are on an absolute scale; they are not shifted in any way. Complementary reflectance data are shown in the Supporting information.

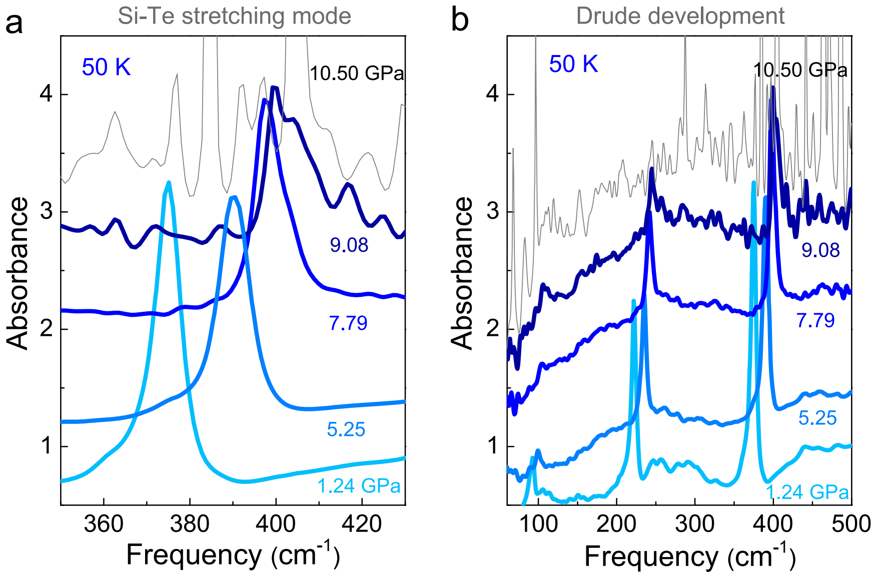

Fig. 2 **Infrared response of $CrSiTe_3$ under extreme pressure–temperature conditions.** **a** Close-up view of the infrared-active Si–Te stretching mode showing the development of the first-order structural phase transition. The two-phase region becomes more sluggish with decreasing temperature. Oscillator fits are available in the Supporting information. **b** Spectral evidence for the insulator–metal transition due to closure of the indirect gap. The background is rising, and the phonons rise incompletely screened on top of the metallic background until the indirect gap closes and the signature of the phonons disappears due to screening by the Drude (indicated in gray). These spectra are on an absolute scale; they are not shifted in any way.

same range[27]. We therefore attribute the broadening and subsequent weak doublet character of the Si–Te stretching mode to the simultaneous presence of two slightly different structural phases between approximately 6 and 8 GPa. $CrSiTe_3$ therefore goes from $R\bar{3}$ → a two phase region that is a combination of $R\bar{3}$ + the high-pressure phase → a high-pressure phase that is slightly different from $R\bar{3}$. The mixed-phase regime is relatively narrow at room temperature, and the subsequent high-pressure structure does not last long in isolation. In fact, the appearance of this phase almost immediately triggers the insulator–metal transition. Based upon room temperature x-ray diffraction[27], the structure of the high-pressure and metallic phases are probably the same. A similar scenario in terms of transition primacy plays out in $FePS_3$[16].

Metallicity in $CrSiTe_3$ develops gradually at room temperature. The absorption background rises with increasing pressure, and the phonons rise partially screened above it until the 0.4 eV indirect gap closes, completely obscuring the phonons [Fig. 1d]. This definition of the onset to the insulator–metal transition is consistent with the gradual maturation of metallicity in the relectance spectra as well. Tracking the development of metallicity in this manner is a much better way to determine the location of the insulator–metal transition than from an inflection point or "hump" in the resisitivity[27]. The "hump method" might work for a direct gap material, but the closure of the indirect gap in $CrSiTe_3$ is more subtle. In our hands, the indirect gap is fully closed, and metallicity is established at 9.5 GPa. We reiterate that it is very clear that the 0.4 eV indirect gap is closing—not the 1.2 eV direct gap[23], because the latter does not move into our frequency window. This makes the system a bad metal. Closure of a direct gap would likely be sharp and strong. There would be no chance of seeing phonons after metallicity sets in due to screening effects. Indirect gap closure, on the other hand, is a very favorable situation, giving a beautiful view of the structural transition and gradual evolution of metallicity.

Tracking these transitions to lower temperatures

$CrSiTe_3$ hosts a similar pattern of phonons at lower temperatures, and the three infrared-active vibrational modes get sharper due to lifetime effects. The two-phase region (consisting of $R\bar{3}$ and a higher pressure phase with slightly different structure) broadens considerably and becomes more sluggish with decreasing temperature. Metallicity appears only after the structural phase transition is complete—typically near 9.5 GPa. At 100 K, the insulator–metal transition is above 10 GPa, indicating that the phase boundary is moving outward. The trend is even stronger at 50 K [Fig. 2], and the mixed phase persists over a wider pressure range than before. Even so, the structural phase transition is always complete before the insulator–metal transition takes place and once it is resolved, metallicity arises almost immediately. Each step is an independent process, and the sequence is invariably the same: $R\bar{3}$ → mixed phases → high pressure structural phase → insulator–metal transition. This progression is exactly opposite of what is reported in ref. [27].

The space group in the narrow high-pressure region between the structural phase transition and the insulator–metal transition is also of interest. Unfortunately, the phonons are heavily screened in this bad metal region, making it difficult to analyze symmetry breaking and carry out a subgroup analysis[20,22]. We can, however, state that the high-pressure vibrational properties of $CrSiTe_3$ above the two-phase region are inconsistent with the $R3$ space group that has been proposed for $CrGeTe_3$[7] because the infrared spectra of $CrSiTe_3$ provide no evidence for a loss of the inversion center which is expected for a transition to a polar space group. Clearly, more effort is needed to reveal the symmetry and properties of $CrSiTe_3$ above the structural phase transition.

Developing the temperature–pressure phase diagram

Figure 3 displays the T–P phase diagram of $CrSiTe_3$, created by bringing together spectroscopic information about the structural and insulator–metal transitions described above with selected data on the pressure dependence of the Curie and superconducting transition temperatures from ref. [27]. The overall character of the phase diagram is quite different from the previous report[27] especially in terms of the sequence of the structural and insulator–metal phase transitions and the shape of the phase boundaries. In our hands, the structural transition is

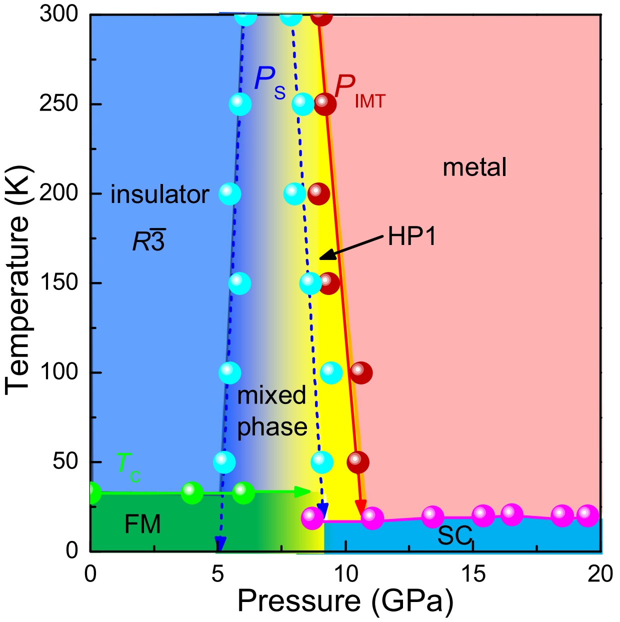

Fig. 3 Phase diagram of $CrSiTe_3$. Temperature–pressure phase diagram summarizing the structural, magnetic, and electronic properties of $CrSiTe_3$. The beginning and end of the structural phase transition as well as the position of the insulator–metal transition are determined from the spectroscopic results discussed here. The Curie temperature and the superconducting transition temperature (×5) as a function of pressure are from ref. [27].

initiated and fully complete before the insulator–metal transition takes place, and metallicity is due to the closure of the indirect gap. We know that the direct gap is still open at 10 GPa because we do not see it come into our spectral range at these pressures. Closure of the direct gap takes place at higher pressure.

As indicated on the *T*–*P* phase diagram, the insulator–metal phase boundary occurs after the structural phase transition—not before—and it moves to higher pressure with decreasing temperature. Therefore the slope of $\partial T/\partial P$ is negative rather than positive as previously supposed[27]. From a thermodynamic point of view, this means that changes in volume and entropy have opposite signs. Since the volume change ΔV is likely ≤ 0 under compression, the change in entropy ΔS is probably ≥ 0[37]. In other words, entropy increases across the insulator–metal transition. Similar trends are observed in $1T\text{-}TiSe_2$[38]. By contrast, the two-phase region of the structural phase transition broadens with decreasing temperature. That the mixed phase region is larger at low temperatures might be due to non-hydrostaticity, but it is more likely a consequence of the first-order transition exhibiting a wider hysteresis. Even so, the structural phase transition is much more involved in the development of superconductivity than previously believed. At the lowest temperatures that we could reach while still increasing pressure in situ, both the structural and insulator–metal transitions occur in quick succession and seem to be in very close proximity to a number of competing states including superconductivity. This intersection of states suggests that a quantum critical point may reside in the vicinity. While we can not say anything specific about the superconducting state in $CrSiTe_3$, we now better understand the sequence of events leading up to superconductivity. In fact, it may turn out that the insulator–metal transition directly triggers superconductivity at low temperature.

Toward pressure effects in the two-dimensional limit

Thus far, we measured the far infrared response of $CrSiTe_3$ under extreme pressure–temperature conditions in order to reveal how pressure controls the interplay between the structural phase transition, the insulator–metal transition, ferromagnetism, and superconductivity in a complex chalcogenide. We find that the insulator–metal transition is triggered by the structural phase transition almost immediately—once the sluggish mixed-phase region is eliminated. Furthermore, the structural transition widens with decreasing temperature, and the slope of the insulator–metal transition is consistent with increasing entropy. These trends change completely the character of the *T*–*P* phase diagram and lead to a critical nexus of activity that may hide a quantum critical point and allow superconductivity to emerge at low temperature. Extension of the *T*–*P* phase diagram toward the few- and single-sheet limit is highly desirable. There is already evidence in other systems such as FeSe and TaS_2 that the superconducting transition temperature T_C increases in the ultrathin limit[35,36]. Here, it is important to use a technique that can accurately identify closure of the indirect gap. As we discuss, *dc* conductivity is not very good for establishing the insulator–metal transition in $CrSiTe_3$, but it should be ideal for identifying the superconducting transition. Infrared techniques by contrast are superb for tracking the structural and insulator–metal transitions in $CrSiTe_3$ but will probably be less successful following the transition to the superconducting state. In principle, infrared spectroscopy can see the gap open (if the system is *s*-wave), but it will be challenging to see a superconducting gap develop inside a diamond anvil cell at low temperature and in the ultrathin limit. Techniques based upon relative slope changes in the reflectance may be successful if electron-phonon processes are relevant[39]. Beyond unraveling the sequence of transitions that trigger superconductivity in $CrSiTe_3$, the ability to control complex chalcogenides under pressure will advance the science base and support the development of high-performance photoresponsive devices and efficient hydrogen storage[40,41].

METHODS

Crystal growth and loading the diamond anvil cell

High-quality $CrSiTe_3$ single crystals were grown via flux techniques as described previously[23]. A small, well-shaped piece of the crystal was selected and loaded into a suitably-chosen diamond anvil cell with a hydrocarbon grease (petroleum jelly) pressure medium to ensure quasi-hydrostatic pressure conditions and an annealed ruby ball to determine pressure via fluorescence[42]. The synthetic type IIas diamonds in the symmetric diamond anvil cell had 500 μm culets, and we employed a 47 μm thick pre-indented stainless steel gasket with a 200 μm hole diameter. Care was taken to optimize optical density in order to reveal the features of interest.

Synchrotron-based infrared spectroscopy under extreme conditions

Taking advantage of the stable, high-brightness beam, synchrotron-based infrared spectroscopy (60-680 cm^{-1}; 4 cm^{-1} resolution; both transmittance and reflectance geometries) was performed using the 22-IR-1 beamline at the National Synchrotron Light Source II at Brookhaven National Laboratory. Absorbance is calculated as $\alpha(\omega) = -\ln(\mathcal{T}(\omega))$, where $\mathcal{T}(\omega)$ is the measured transmittance. The pressure was increased between 0 and 11 GPa—first at room temperature and then at several lower temperatures using a custom-built cryostat that accomodates the diamond anvil cell and supports in situ compression measurements. For the low-temperature experiments, one ruby ball was positioned inside the sample chamber while another was placed on the diamond backplate as a temperature reference[42]. We also monitored the shape of the ruby fluorescence spectrum to ensure that the sample remained in a quasi-hydrostatic environment. Although an open flow system, this cryostat is limited to work above approximately 50 K in order to control the step size during isothermal compression of the diamond anvil cell. Our protocol for determining the position of each phase transition was developed at room temperature (as described in the Supporting information) and then extended to low temperature. The phase transitions are fully reversible upon the release of pressure at each temperature. Further, recompression of the same crystal and then release gives the same results, so we can be confident that crystal quality remains high under these extreme pressure–temperature conditions.

DATA AVAILABILITY

Data are available from the corresponding author upon reasonable request.

Received: 19 September 2022; Accepted: 10 March 2023;
Published online: 07 April 2023

REFERENCES

1. Zallen, R. Effect of pressure on optical properties of crystalline As_2S_3. *High Pres. Res.* **24**, 117 (2004).
2. Wang, Y. et al. Pressure-driven cooperative spin-crossover, large-volume collapse, and semiconductor-to-metal transition in manganese(II) honeycomb lattices. *J. Am. Chem. Soc.* **138**, 15751 (2016).
3. Haines, C. et al. Pressure-induced electronic and structural phase evolution in the van der Waals compound $FePS_3$. *Phys. Rev. Lett.* **121**, 266801 (2018).
4. Wang, Y. et al. Emergent superconductivity in an iron-based honeycomb lattice initiated by pressure-driven spin-crossover. *Nat. Commun.* **9**, 1914 (2018).
5. Coak, M. J. et al. Isostructural Mott transition in 2D honeycomb antiferromagnet $V_{0.9}PS_3$. *npj Quant. Mater.* **4**, 38 (2019).
6. Zheng, Y., Jiang, X. X., Xue, X. X., Dai, J. & Feng, Y. Ab initio study of pressure-driven phase transition in $FePS_3$ and $FePSe_3$. *Phys. Rev. B* **100**, 174102 (2019).
7. Yu, Z. et al. Pressure-induced structural phase transition and a special amorphization phase of two-dimensional ferromagnetic semiconductor $Cr_2Ge_2Te_6$. *J. Phys. Chem. C* **123**, 13885–13891 (2019).
8. Kim, H. S., Haule, K. & Vanderbilt, D. Mott metal-insulator transitions in pressurized layered trichalcogenides. *Phys. Rev. Lett.* **123**, 236401 (2019).
9. Wang, X. et al. Current-driven magnetization switching in a van der Waals ferromagnet Fe_3GeTe_2. *Sci. Adv.* **5**, eaaw8904 (2019).
10. Susilo, R. A. et al. Band gap crossover and insulator-metal transition in the compressed layered $CrPS_4$. *npj Quant. Mater.* **5**, 58 (2020).
11. Coak, M. J. et al. Tuning dimensionality in van-der-Waals antiferromagnetic Mott insulators $TMPS_3$. *J. Phys.: Condens. Matter* **32**, 124003 (2020).
12. Harms, N. C. et al. Piezochromism in the magnetic chalcogenide $MnPS_3$. *npj Quant. Mater.* **5**, 56 (2020).
13. Kang, S. et al. Coherent many-body exciton in van der Waals antiferromagnet $NiPS_3$. *Nature* **583**, 785–789 (2020).
14. Wildes, A. R. et al. High field magnetization of $FePS_3$. *Phys. Rev. B* **101**, 024415 (2020).
15. Ma, X. et al. Dimensional crossover tuned by pressure in the layered magnetic $NiPS_3$. *Sci. China Phys. Mech. Astron.* **64**, 297011 (2021).
16. Coak, M. J. et al. Emergent magnetic phases in pressure-tuned van der Waals antiferromagnet $FePS_3$. *Phys. Rev. X* **11**, 011024 (2021).
17. Kim, M., Kim, H.-S., Haule, K. & Vanderbilt, D. Orbital-selective Mott phase and non-Fermi liquid in $FePS_3$. *Phys. Rev. B* **105**, L041108 (2022).
18. Zhu, F. F. et al. Topological magnon insulators in two-dimensional van der Waals ferromagnets $CrSiT_3$ and $CrGeTe_3$: Toward intrinsic gap-tunability. *Sci. Adv.* **7**, eabi7532 (2021).
19. Mai, T. T. et al. Magnon-phonon hybridization in 2D antiferromagnet $MnPSe_3$. *Sci. Adv.* **7**, eabj3106 (2021).
20. Harms, N. C. et al. Symmetry progression and polar metallicity in $NiPS_3$ under pressure. *npj 2D Mater. Appl.* **6**, 40 (2022).
21. Zhao, H. et al. Mechanical control of physical properties in the van der Waals ferromagnet $Cr_2Ge_2Te_6$ via application of electric current. *Phys. Rev. B* **106**, L041103 (2022).
22. Harms, N. C. et al. Metal site substitution and the role of the P-P dimer on symmetry breaking in $FePS_3$ and $CrPS_4$. *ACS Appl. Elect. Mater.* **4**, 3246 (2022).
23. Casto, L. D. et al. Strong spin-lattice coupling in $CrSiTe_3$. *Appl. Phys. Lett. Mater.* **3**, 041515 (2015).
24. Williams, T. J. et al. Magnetic correlations in the quasi-two-dimensional semiconducting ferromagnet $CrSiTe_3$. *Phys. Rev. B* **92**, 144404 (2015).
25. Liu, B. et al. Critical behavior of the quasi-two-dimensional semiconducting ferromagnet $CrSiTe_3$. *Sci. Rep.* **6**, 33873 (2016).
26. Gong, C. et al. Discovery of intrinsic ferromagnetism in two-dimensional van der Waals crystals. *Nature* **546**, 265–269 (2017).
27. Cai, W. et al. Pressure-induced superconductivity and structural transition in ferromagnetic $CrSiTe_3$. *Phys. Rev. B* **102**, 144525 (2020).
28. Lebegue, S., Bjorkman, T., Klintenberg, M., Nieminen, R. & Eriksson, O. Two-dimensional materials from data filtering and ab initio calculations. *Phys. Rev. X* **3**, 31002 (2013).
29. Li, X. & Yang, J. $CrXTe_3$ ($X = Si, Ge$) nanosheets: two dimensional intrinsic ferromagnetic semiconductors. *J. Mater. Chem. C* **2**, 7071–7076 (2014).
30. Chen, X., Qi, J. & Shi, D. Strain-engineering of magnetic coupling in two-dimensional magnetic semiconductor $CrSiTe_3$: Competition of direct exchange interaction and superexchange interaction. *Phys. Lett. A* **379**, 60–63 (2015).
31. Lin, M.-W. et al. Ultrathin nanosheets of $CrSiTe_3$: a semiconducting two-dimensional ferromagnetic material. *J. Mater. Chem. C* **4**, 315–322 (2016).
32. Zhang, J.-M., Nie, Y.-Z., Xia, Q.-L., Xiong, R. & Guo, G.-H. Electronic structures and magnetic properties of $CrSiTe_3$ single-layer nanoribbons. *Phys. Lett. A* **383**, 2346–2351 (2019).
33. Ron, A. et al. Unltrafast enhancement of ferromagnetic spin exchange induced by ligand-to-metal charge transfer. *Phys. Rev. Lett.* **125**, 197203 (2020).
34. Zhang, C. et al. Pressure-enhanced ferromagnetism in layered $CrSiTe_3$ flakes. *Nano Lett.* **21**, 7946–7952 (2021).
35. Navarro-Moratalla, E. et al. Enhanced superconductivity in atomically thin TaS_2. *Nature Commun.* **7**, 11043 (2016).
36. Shigekawa, K. et al. Dichotomy of superconductivity between monolayer FeS and FeSe. *Proc. Nat. Acad. Sci.* **116**, 24470 (2019).
37. Smith, K. A. et al. Revealing pressure-driven structural transitions in the hybrid improper ferroelectric $Sr_3Sn_2O_7$. *Phys. Rev. B* **104**, 064106 (2021).
38. Kusmartzeva, A. F., Sipos, B., Berger, H., Forró, L. & Tutis, E. Pressure induced superconductivity in pristine 1T-$TiSe_2$. *Phys. Rev. Lett.* **103**, 236401 (2009).
39. Carbotte, J. P., Nicol, E. J. & Timusk, T. Detecting superconducting in the high pressure hydrides and metallic hydrogen from optical properties. *Phys. Rev. Lett.* **121**, 047002 (2018).
40. Ramos, M. et al. Ultra-broad spectra photo-response in $FePS_3$ air stable devices. *npj 2D Mater. Appl.* **5**, 19 (2021).
41. Rezaie, A. A., Lee, E., Luong, D., Yapo, J. A. & Fokwa, B. P. T. Abundant active sites on the basal plane and edges of layered van de Waals Fe_3GeTe_2 for highly efficient hydrogen evolution. *ACS Mater. Lett.* **3**, 313 (2021).
42. Mao, H. K., Bell, P. M., Shaner, J. W. & Steinberg, D. J. Specific volume measurements of Cu, Mo, Pd, and Ag and calibration of the ruby R_1 fluorescence pressure gauge from 0.06 to 1 Mbar. *J. Appl. Phys.* **49**, 3276 (1976).

ACKNOWLEDGEMENTS

J.L.M. appreciates funding from Physical Behavior of Materials, Basic Energy Sciences, U.S. Department of Energy (Contract number DE-SC00023144). D.M. acknowledges support from the Gordon and Betty Moore Foundation's EPiQS Initiative, Grant GBMF9069. Work at the National Synchrotron Light Source II at Brookhaven National Laboratory is funded by the Department of Energy (DE-AC98-06CH10886). Use of the 22-IR-1 beamline is supported by COMPRES, the Consortium for Materials Properties Research in Earth Sciences, under NSF Cooperative Agreement EAR 1606856 and CDAC (DE-NA0003975). We thank S. N. Neal, K. Park, and K. A. Smith for useful conversations.

AUTHOR CONTRIBUTIONS

J.L.M. designed the study. D.M. grew the crystals. J.L.M. and Z.L. performed the high pressure measurements. J.L.M. analyzed the spectral data and wrote the manuscript. All authors commented on the text.

COMPETING INTERESTS

The authors declare no competing interests.

ADDITIONAL INFORMATION

Supplementary information The online version contains supplementary material available at https://doi.org/10.1038/s41699-023-00389-x.

Correspondence and requests for materials should be addressed to J. L. Musfeldt.

Reprints and permission information is available at http://www.nature.com/reprints

Publisher's note Springer Nature remains neutral with regard to jurisdictional claims in published maps and institutional affiliations.

Open Access This article is licensed under a Creative Commons Attribution 4.0 International License, which permits use, sharing, adaptation, distribution and reproduction in any medium or format, as long as you give appropriate credit to the original author(s) and the source, provide a link to the Creative Commons license, and indicate if changes were made. The images or other third party material in this article are included in the article's Creative Commons license, unless indicated otherwise in a credit line to the material. If material is not included in the article's Creative Commons license and your intended use is not permitted by statutory regulation or exceeds the permitted use, you will need to obtain permission directly from the copyright holder. To view a copy of this license, visit http://creativecommons.org/licenses/by/4.0/.

© The Author(s) 2023